Relating Carrier Dynamics and Photovoltaic Device Performance of a CZTSe Single Crystal

Siming Li,[1] Michael A. Lloyd,[2] Hannes Hempel,[3] Charles J. Hages,[3] José A. Márquez,[3] Thomas Unold,[3] Rainer Eichberger,[4] Brian E. McCandless,[2] Jason B. Baxter[1]

[1] Drexel University, Department of Chemical and Biological Engineering, Philadelphia, PA, 19104, USA

[2] University of Delaware, Institute of Energy Conversion, Newark, DE, 19716, USA

[3] Department of Structure and Dynamics of Materials, Helmholtz-Zentrum Berlin für Materialien und Energie GmbH, 14109 Berlin, Germany

[4] Institute for Solar Fuels, Helmholtz-Zentrum Berlin für Materialien und Energie GmbH, 14109 Berlin, Germany

ABSTRACT

Understanding the relationship of photoexcited carrier lifetimes, mobilities, and recombination mechanisms to structural properties and processing of photovoltaic (PV) absorber materials is critical to the design of efficient solar cells. Carrier dynamics in PV absorbers have conventionally been characterized by time-resolved photoluminescence (TRPL), but TRPL may not be suitable or straightforward for all absorbers. Alternative non-contact methods can enable measurement of ultrafast carrier dynamics for a wider range of materials. Here we demonstrate the complementary use of time-resolved terahertz spectroscopy (TRTS) and near-infrared transient reflectance (NIR-TR) spectroscopy along with TRPL to elucidate photoexcited carrier dynamics in a high-quality copper-poor, zinc-rich kesterite $Cu_2ZnSnSe_4$ (CZTSe) single crystal. The single-crystalline nature of the sample eliminates complications arising from grain boundaries, secondary phases, and interfaces associated with thin film growth. A single-crystal-based PV device exhibited an efficiency of 6.2% and V_{oc} of 400 mV, consistent with the quasi-Fermi level splitting determined using absolute photoluminescence. NIR-TR showed picosecond-scale cooling and relaxation of carriers into a distribution of band tail states while TRTS revealed a characteristic time scale of 200 – 260 ps for recombination. Hall effect and TRTS measurements revealed electron and hole mobilities in the range of 50 – 100 cm^2/Vs. These dynamics result in a characteristic minority carrier diffusion length of less than 200 nm, leading to incomplete carrier collection, as confirmed by a strongly decreasing external quantum efficiency at long wavelengths. Our approach combining ultrafast spectroscopy and device measurements can lead to more detailed

understanding of performance-limiting photophysical processes and can accelerate the development of more efficient PVs.

I. INTRODUCTION

Ultrafast spectroscopy enables non-contact measurement of charge carrier dynamics that link photoexcited carrier lifetimes, recombination mechanisms, and mobilities to the structure and processing of photovoltaic (PV) absorber materials and ultimately to device performance [1-4]. This understanding is critical to the design of efficient solar cells but is inherently compromised by inadequate knowledge of all necessary material properties. This challenge is even more formidable in thin films, which in addition to interfaces, inherently suffer from heterogeneity from grain boundaries and possible secondary phases. Time-resolved photoluminescence (TRPL) has been the standard method for measuring photoexcited carrier lifetimes in thin film photovoltaic absorbers [4-7]. However, conventional TRPL in the IR range often has an instrument response function of hundreds of picoseconds which may be close to the expected carrier lifetime in un-optimized materials.

Here, we use TRPL as well as complementary near infrared transient reflectance spectroscopy (NIR-TR) and time-resolved terahertz spectroscopy (TRTS) to measure dynamics of a kesterite $Cu_2ZnSnSe_4$ (CZTSe) single crystal. Optical transient reflectance and transient absorption measure the dynamics of interband transitions and provide information on carrier relaxation and distribution within the band structure [8]. TRTS is a non-contact probe of transient photoconductivity on the sub-picosecond to nanosecond time scales that are relevant for charge carrier generation, transport, and recombination [9-11].

The kesterite-type material $Cu_2ZnSn(S,Se)_4$ (CZTSSe) is a promising candidate for PV applications. It has a direct band gap that is tunable from 1.0-1.5 eV [12, 13] by changing the S:Se ratio, promising theoretical single-junction PV efficiencies above 30% [14]. Moreover, unlike CdTe and $Cu(In,Ga)Se_2$ (CIGS), CZTSSe is composed of non-toxic, Earth-abundant, and inexpensive elements. CZTSSe-based PV devices have reached power conversion efficiencies of 12.6%.[15] However, this efficiency remains low compared both to the theoretical limit and to CdTe and CIGS, which have exceeded 21% [16].

Complex defect chemistry and highly non-equilibrium growth conditions of CZTSSe thin films result in grain boundaries, secondary phases, and point defects, which limit solar cell efficiency [17]. Nanoscale fluctuations in chemical composition, including high densities of Zn_{Cu} and Cu_{Zn} antisite defects and defect clusters, are thought to cause potential fluctuations and band tails that may limit the open circuit voltage (V_{oc}) [18, 19]. The V_{oc} deficit (E_g-V_{oc}) of CZTSSe

devices is in the range of 600 mV - 900 mV depending on bandgap, and the champion device with 12.6% efficiency exhibited a V_{oc} deficit of 617 mV [15, 20-22].

To date, characteristic TRPL decay times for the best CZTSSe films and devices are in the range of 1 – 10 ns [23-28]. However, Hages et al. have recently shown that these TRPL decay times generally do not correspond to the minority carrier lifetime. Instead, these times are likely related to minority carrier de-trapping times, with the true minority carrier lifetimes falling in the range of a few hundred picoseconds [29]. Coupled with mobilities on the order of 100 $cm^2V^{-1}s^{-1}$ [3, 30], the corresponding diffusion length of 0.2 – 2 μm can result in incomplete carrier collection.

Here we report on the photovoltaic properties and carrier dynamics of a CZTSe single crystal with copper-poor, zinc-rich composition (Cu/(Zn+Sn)=0.87, Zn/Sn=1.22) in the range that commonly leads to the highest device efficiencies [31, 32]. We have chosen to study the pure selenide to avoid complications related to anion chemistry. Photoexcited carrier dynamics are sensitive to crystal quality and defects. By investigating a high-quality, quasi-equilibrium single crystal of CZTSe, we eliminate the effects of grain boundaries and minimize the impact of secondary phases. The strategy of studying single crystals to infer routes to improve polycrystalline thin film PV devices has proven to be remarkably effective for CdTe [33, 34], and has recently been employed for CZTSSe as well [35-40]. Notably, Kanemitsu et al. have investigated carrier dynamics in CZTS [35, 36, 38] and CZTSSe [37] single crystals. Their work provides an excellent starting point to understand dynamics, which we build upon here by linking dynamics to detailed physical characterization, device measurements, and modeling. Our finished CZTSe crystal measures 3 mm diameter and 0.87 mm thick and exhibits p-type conduction with Hall mobility of 89 $cm^2V^{-1}s^{-1}$ for holes. A device built upon the crystal attained an efficiency of 6.2%, with V_{oc} of 400 mV and J_{SC} = 28.2 mA/cm^2. NIR-TR reveals picosecond scale cooling and trapping of photoexcited carriers. TRPL and TRTS show characteristic decay times of ~200 ps. A combination of fluence and wavelength dependence studies, coupled with modeling, shows that 1st-order Shockley-Read-Hall recombination is the dominant recombination mechanism in the CZTSe single crystal studied.

II. EXPERIMENTAL METHODS

Crystal Growth and Properties. Ingots of CZTSe material were synthesized at temperatures below the peritectic point of 790 ˚C [41] in a manner outlined by Bishop *et al*. [42]. Elemental precursors of 5-6N purity were loaded into a quartz ampoule, pumped for >12 hours and sealed at a base pressure of 5×10^{-6} torr. CZTSe growth and grain ripening were promoted at 750 ˚C over a 20-day period. The ampoule was allowed to naturally cool within the oven to room temperature over a 36-hour period. Single-crystalline material was extracted from the resulting multicrystalline boule. Crystals were mechanically thinned to a planar surface on one side with diminishing grit sizes of SiC and Al_2O_3 down to a particle size of 0.05 μm. Mechanical damage resulting from the abrasive grinding steps was treated using a 10-minute solution etch of 0.125% bromine in methanol which removes a surface layer approximately four microns thick. The finished crystal of interest in this study was ~3 mm in diameter and 0.87 mm thick. Another crystal of similar composition and thickness of 1.2 - 1.6 mm from the same synthesis was used to obtain Hall measurements.

Crystal composition was determined by x-ray fluorescence spectroscopy (XRF) in air on an Oxford Instruments Xstrata system. X-rays are generated with a Tungsten target with a filament current held at 0.404 mA and an acceleration voltage of 45 kV. An Aluminum 1.5 keV filter was used to harden the primary beam. Probing area was determined by a 1.3 mm collimator. Composition quantification was calibrated to a standard characterized *via* inductively coupled plasma mass spectroscopy.

Majority carrier concentration and mobility were measured by Hall effect in the van der Pauw configuration at room temperature in the dark. Conductivity type was checked by the sign of the Seebeck voltage, obtained by hot probe method, using a tip heated to 220˚C and spacing determined by the size of the crystal (3-4 mm). The linearity of the Seebeck voltage was verified over the probe temperature range from 120˚C to 280˚C. In preparation for Hall effect measurements, the plane-parallel crystal was affixed to the center of a soda lime glass substrate coated with four molybdenum contact pads using Crystalbond® adhesive. Gold wires were attached at equi-spaced positions on the crystal with conductive carbon paste and soldered to molybdenum pads on the glass substrate. DC measurements were made at three current values to evaluate linearity of resistivity, and the magnetic field strength was varied from 5 to 15 kG normal to the crystal surface.

Device Preparation and Efficiency Measurement. After the measurement of carrier dynamics, the crystal was re-planarized via mechanical polishing. An additional chemical-mechanical polish was implemented, consisting of mechanical abrasion on a pad saturated in a 0.125% bromine in methanol solution. The crystal was then re-etched for 10 minutes in the same solution and annealed at 350˚C anneal for 6 minutes in ambient atmosphere. Device fabrication proceeded in a manner outlined in [43] whereby a 60 nm CdS emitter layer was deposited by chemical bath deposition at 65˚C. A 3.15 mm^2 device area was defined by depositing circular ZnO/ITO layer via sputtering. Back contact was obtained by bonding the crystal with Acheson Electrodag® graphite paste to a Mo-coated glass substrate. For all device characterization, electrical contact was made to the Mo for positive contact and directly to the ITO layer for the negative contact.

An OAI TriSOL solar simulator calibrated to 100 $mWcm^{-2}$ via an NREL certified Silicon standard was used for device JV measurements at 25 ˚C. External quantum efficiency (EQE) was measured using an Oriel monochromator from 350 to 1400 nm using AC method with a lock-in amplifier.

Photoluminescence. Hyperspectral PL imaging data was acquired with a custom setup described elsewhere [44]. The excitation was carried out with 660 nm lasers coupled to homogenizer units. The excitation intensity was 4.8 x 10^{21} photons m^{-2} s^{-1}, which is equivalent to ~1.6 suns for a material with a bandgap of 1 eV.

TRPL measurements were performed with 660 nm excitation wavelength using a pulsed laser source with a Gaussian profile excitation spot ca. 30 μm in diameter, at laser pulse frequencies of 500 kHz to 2.5 MHz. The incident photon flux has Gaussian time dependence with pulse length $\tau_p \approx 34$ ps. Detection of wavelength-integrated luminescence utilized time-correlated single photon counting with an InGaAs photomultiplier tube; the instrument response function of the detection is limited to ca. 300 ps. Temperature-dependent measurements were performed in an evacuated closed-cycle He cryostat. Presented TRPL data are background-subtracted and normalized to the peak intensity.

Time-Resolved Terahertz Spectroscopy. TRTS was performed with a regeneratively amplified Ti: Sapphire laser (Coherent RegA, center wavelength of 800 nm, pulse duration of 70 fs, and repetition rate of 150 kHz) coupled to a home-built reflectance spectrometer. Transmission

geometry could not be used at room temperature because of the large thickness and moderate conductivity of the crystal. The reflection TRTS configuration and analysis has been described in more detail elsewhere [30]. The sample was excited with a 400 nm or 800 nm pump pulse, then probed at delay times up to 2 ns with terahertz radiation generated and detected using ZnTe nonlinear crystals. For TRTS photoconductivity measurements, the change in reflectance upon chopped photoexcitation was normalized by the non-photoexcited signal to determine $\Delta R/R$.

Near Infrared Transient Reflectance Spectroscopy. NIR-TR spectroscopy was performed using a Ti:Sapphire laser (Spectra-Physics Spitfire) coupled to an optical parametric amplifier to control the pump photon energy and to a TR spectrometer (Ultrafast Systems, Helios). Spectral response was monitored from 900 – 1600 nm using a white light continuum probe generated by focusing the 800 nm seed pulse into a sapphire crystal and detected by an InGaAs multichannel detector. Differential absorbance was probed over the first 3 ns after photoexcitation. The delay time was controlled by an optical delay line. The sample was excited with 400 nm photons at 13 μJ/cm^2.

Modeling Transport and Recombination. We solved the time-dependent continuity equation (Eq. 1) to model carrier transport and recombination. We assume that no electric fields exist within the domain of interest, so that photoexcited electron and hole profiles are identical and carriers move according to their ambipolar mobility. The initial distribution of photoexcited carriers follows an exponential decay profile based on Beer's Law (Eq. 2). The absorption coefficients for 400 nm and 800 nm photons are 2×10^5 cm^{-1} and 6×10^4 cm^{-1}, respectively, which were obtained from ellipsometry data for a CZTSe single crystal of similar composition [45]. With a carrier mobility of 80 cm^2/Vs and lifetime of 200 ps, the diffusion length is 200 nm, which is similar to the optical penetration depth but significantly smaller than the thickness of the crystal (0.87 mm). Therefore, boundary conditions include front surface recombination (Eq. 3) while rear surface effects may be ignored. To reduce computation time compared to simulating the entire crystal thickness, we instead set the carrier flux to zero at a pseudo-boundary at $x=10L_D$ as the other boundary condition (Eq. 4).

Continuity Eqn: $$\frac{\partial \Delta n(x,t)}{\partial t} = D\frac{\partial^2 \Delta n}{\partial x^2} - k_{SRH}\Delta n - k_{rad}\Delta n^2 - k_{Aug}\Delta n^3 \qquad (1)$$

Initial Condition: $$\Delta n(x,0) = \Delta n_0 \exp(-\alpha x) \qquad (2)$$

Boundary Conditions: $$\frac{\partial \Delta n(x,t)}{\partial x}|_{x=0} = \frac{SRV_{front}}{D}\Delta n(0,t) \quad (3)$$

$$\frac{\partial \Delta n(x,t)}{\partial x}|_{x=10L_D} = 0 \quad (4)$$

Here D is the ambipolar diffusion coefficient, k_{SRH}, k_{rad} and k_{Aug} are recombination rate constants for Shockley-Read-Hall, radiative, and Auger mechanisms, respectively, α is the absorption coefficient, and SRV is the front surface recombination velocity. We assume that TRTS signal is proportional to the integrated Δn within the whole effective thickness ($10L_D$).

III. RESULT & DISCUSSION

The single crystal under investigation had a Cu/(Zn+Sn) ratio of 0.87, and Zn/Sn ratio of 1.22 as measured by XRF. This crystal composition falls within the Cu-poor, Zn-rich regime known to produce optimal efficiency in CZTSSe thin film devices [31, 32]. The single crystal used in this study yielded a photovoltaic device with an efficiency of 6.2%, as shown in **Figure 1(a)**, with device parameters of V_{oc} = 400 mV, J_{sc} = 28.2 mAcm^{-2}, and FF = 54.6%. The demonstrated V_{oc}, is comparable to state-of-the-art CZTSe thin film photovoltaics [15]. The J_{SC} is low compared to that expected for an absorber in this structure and is primarily due to the cell's spectral response. **Figure 1(b)** shows the external quantum efficiency spectrum of the cell, which peaks near 600 nm and falls off at longer wavelengths. Analysis of the long-wavelength cutoff yields an optical band gap of 0.98 eV, consistent with direct measurements we have made on a crystal thinned to 60 microns. The thickness of the cell crystal should allow for the absorption of all non-reflected photons above the bandgap. Therefore, the decrease in EQE at photon energies approaching the band gap indicates that the photocurrent is limited by collection of minority carriers generated further from the junction, which depends on minority carrier lifetime and mobility. The cell fill factor is a lumped parameter containing recombination contributions from the dark diode and parasitic effects due to series resistance and shunt conductance. An analysis of the dark and light diode curves is more fully described in the Supplemental Material section.

The van der Pauw Hall effect was measured in the dark on a crystal of similar composition taken from the same synthesis. The crystal exhibited strong p-type conduction, with resistivity of

0.8 Ω-cm and positive Seebeck coefficient of 0.27 mV/K. The hole density of 8.7×10^{16} cm^{-3} is consistent with doping concentrations achieved in previous reports under the same ratio of Zn/Sn [25]. The hole mobility observed from the Hall effect measurement was determined to be 89 ± 9 cm^2/Vs, which is 10 times higher than that previously reported for CZTSe thin films [46, 47] and a CZTS single crystal [39]. The Hall effect measurement provides DC conductivity of the crystal in the dark, so it is only sensitive to majority carriers. In contrast, TRPL, TRTS, and NIR-TR dynamics depend on both minority and majority carrier mobility.

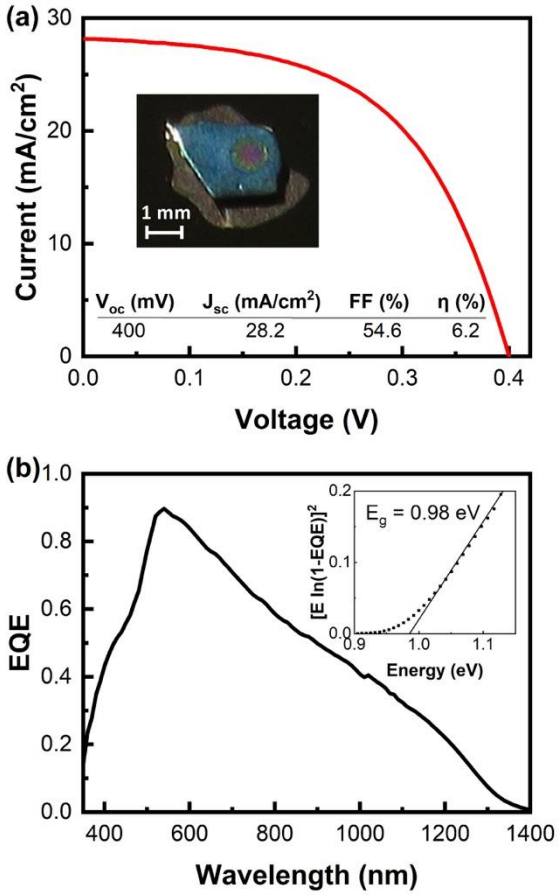

Figure 1. (a) J-V curve under 1 sun (AM 1.5G) illumination. The inset shows a photograph of the single-crystal device. (b) External quantum efficiency showing decreasing carrier collection at longer wavelengths. The inset shows how the band gap of 0.98 eV is obtained from EQE data.

Quantitative hyperspectral PL imaging was used to map the optoelectronic properties of the single crystal. **Figure 2(a)** shows the map of the external PL quantum yield (PLQY) (percentage of emitted photons with respect to the absorbed photons), demonstrating good

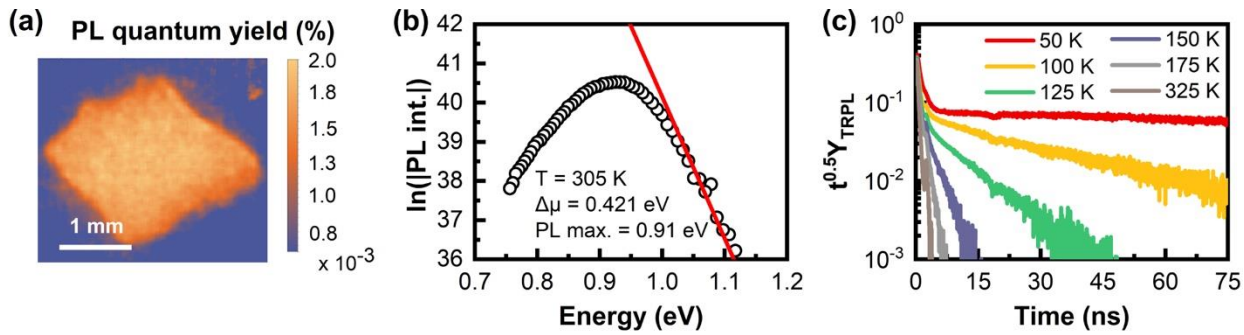

Figure 2. (a) 2D mapping of the PL quantum yield of the crystal at equivalent one sun illumination. (b) Average absolute PL spectrum of the crystal. The red line is the model fitted to the high energy slope of the PL used to calculate the quasi-Fermi level splitting (Δμ). (c) $t^{0.5}Y_{TRPL}$ of the crystal for temperatures between 325 K (fastest decay) and 50 K (slowest decay). TRPL measured wavelength-integrated photoluminescence.

uniformity across the whole crystal. Low-temperature PL (not shown) shows broad Quasi-Donor-Acceptor pair transitions confirming that the crystal is highly compensated, and in this way it is not significantly different from typical polycrystalline CZTS thin films [48]. Histograms representing the PL quantum yield and energy of the maximum of the luminescence from the crystal can be found in the Supplemental Material (**Figure S2(a,b)**). **Figure 2(b)** shows the average room temperature PL spectrum of the crystal on a logarithmic absolute scale. The maximum of the PL peak is at 0.91 eV, indicating that the emission possibly arises from a band-to-impurity transition [49] since the bandgap of the CTZSe single crystal is 0.98 eV as calculated from the EQE measurement. A quasi-Fermi level splitting value of 421 ± 14 meV is calculated from the high-energy slope of the PL spectrum (**Figure 2(b)**) using the method described in Ref. [50]. The calculated quasi-Fermi level splitting represents the maximum V_{oc} that this material could exhibit in a solar cell. With this crystal the calculated quasi-Fermi level splitting is similar to the V_{oc} achieved in the device, indicating that V_{oc}, and thus the performance of this device, might be limited by the bulk properties of the CZTSe.

The device EQE, which limits J_{SC}, shows poor carrier collection beyond 600 nm, suggesting short carrier lifetime. TRPL was used to obtain a first estimate of the bulk minority carrier decay time. To determine this characteristic time from TRPL in a thick film/bulk crystal, carrier diffusion from the initial generation profile into the bulk must be accounted for – particularly in the presence of surface recombination [51]. The bulk decay time τ_{Bulk} in a crystal at long delay times follows $Y_{TRPL}(t) \propto t^{-0.5}e^{-t/\tau Bulk}$ [52]. This is in contrast to the common thin-film

formulation where the decay follows a simple exponential at long decay times. Therefore, for a thick single crystal τ_{Bulk} can be extracted from a plot of $t^{0.5}Y_{TRPL}(t)$, where the data approaches an exponential decay following initial carrier redistribution effects. Accordingly, the TRPL decay was measured over a range of temperatures; experimental data is shown in **Figure 2(c)** for temperatures between 50 K and 325 K, where we find excellent agreement with the theoretically derived decay for a bulk crystal. At early delay times (t < 5 ns) a rapid decay is observed at all temperatures, while $t^{0.5}Y_{TRPL}(t)$ follows an exponential decay at long delay times.

TRPL analysis of the single crystal indicates a fast minority carrier decay time (< 1 ns) for temperatures above 200 K. This result agrees with previous reports of a short bulk minority carrier decay times in kesterite absorbers [29]. At room temperature, an accurate decay time cannot be resolved from TRPL because the decay time is below the time-resolution of the detection system (~300 ps). Below 200 K a rapid increase in the decay time is observed, reaching 400 ns at 25 K; the temperature dependence of τ_{Bulk} is shown in the Supplemental Material (**Figure S2(c)**). While the temperature dependence of τ_{Bulk} does not strictly follow a simple formulation for thermal emission of carriers from a trap state, we nonetheless associate such a strong temperature-dependence of τ_{Bulk} with detrapping of minority carriers in kesterites [29]. The initial rapid decay of carriers for t < 5 ns can be related to recombination and/or redistribution of carriers spatially and within trap states. These results make accurate distinction between carrier trapping/localization times and the minority carrier lifetime difficult from TRPL analysis alone.

To further distinguish carrier cooling, trapping, and recombination, we measured NIR-TR on the same single crystal. The near-IR probe enables interrogation of the near-band edge carriers with an effective detection depth of $\sim\frac{\lambda}{4\pi n}$ [53], which corresponds to ~36 nm near the CZTSe bandgap. In the band gap region, the reflectivity change contains contributions from carrier effects such as band-filling and band gap renormalization and from heating [54-56].

Figure 3(a) shows a 2D plot of the NIR-TR data as a function of both probe energy and pump-probe delay time. **Figure 3(b)** displays the evolution of the NIR-TR spectra with a series of 1-D slices of the data at different pump-probe delay times. The near-band edge feature increases in magnitude and redshifts over the first 1 – 2 ps, which is attributed to cooling of hot carriers. This assignment and time scale is consistent with that previously reported for pure sulfide CZTS single crystals [36]. The feature shifts below the band edge, which we attribute to relaxation of

carriers into potential wells and shallow traps states within the band tails, consistent with the band-to-impurity PL peak emission of 0.91 eV. After reaching a maximum at ~2 ps, the magnitude of this feature decreases over tens to hundreds of picoseconds due to a combination of carrier loss from the band edges by recombination, diffusion out of the probe depth, and deep trapping.

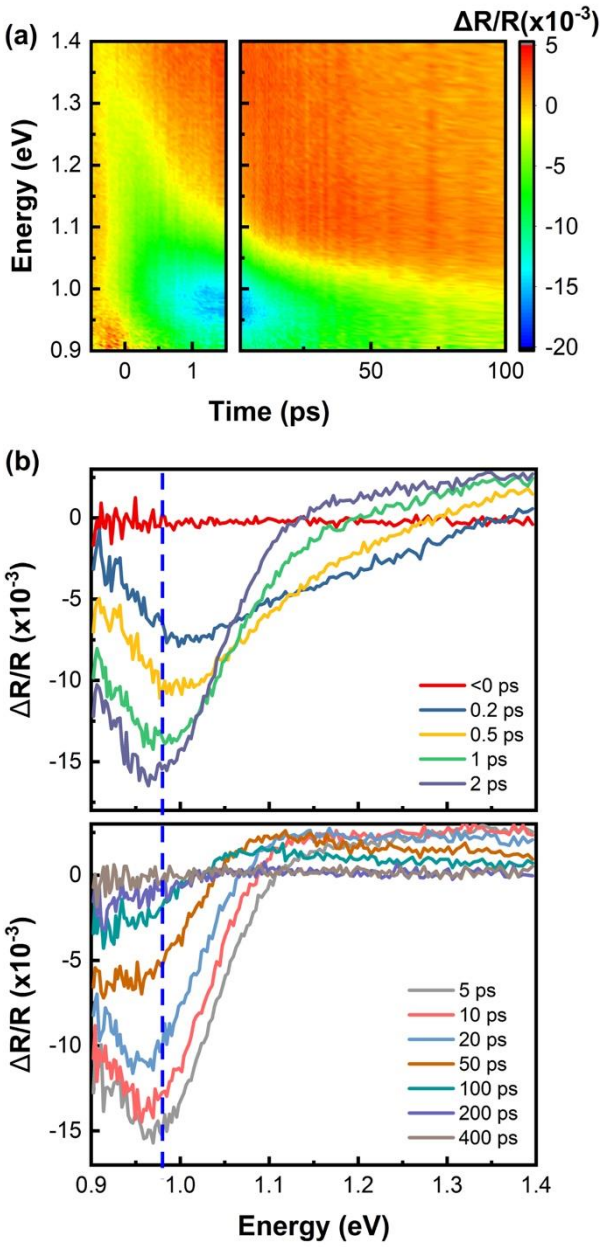

Figure 3. (a) 2D plot of NIR-TR spectra of the crystal. (b) NIR-TR spectra of the crystal at several pump-probe delay times. The total absorbed fluence was 13 μJ/cm^2 with 370 nm photons (photon flux of 2 x 10^{13} cm^{-2}), which gives N_0 = 3 x 10^{18} cm^{-3} within the 36-nm probe depth.

Carrier cooling and non-radiative recombination transfer energy to the lattice, which affects the reflectivity both above and below the band gap due to the temperature dependence of the refractive index [58]. Recent work on oxide thin films has illustrated the important, and often dominant, effect of temperature on TR response [56, 59]. However, thermal effects do not appear

to play a significant role here. Our calculated temperature rise is 0.7 K, which would give rise to thermal features 10-100x smaller [58] than those observed here, as shown in **Figure S3** and described in associated Supplementary Material. We conclude that the feature below the band gap is primarily due to carriers within the band tails.

We used TRTS to gain additional insight into the dynamics and recombination mechanisms of photoexcited carriers. TRTS is an excellent complement to TRPL and NIR-TR because it probes mobile carriers and is not limited to the near-surface region. TRTS reports the time-resolved sheet photoconductivity $\Delta\sigma_S(t_p)$ of the CZTSe crystal and subsequently the decay of the photo-induced sheet carrier concentration Δn_s and mobility μ_{e+h} of the photoexcited electrons and holes.

To this end, TRTS measures the change in the reflection of a terahertz probe pulse, ΔR/R, that is induced by photoexciting the sample with a pump pulse. This change in reflection is described by the so-called "thin film approximation" in equation (5),

$$\Delta\sigma_S(t_p) = q\Delta n_S(t_p)\mu_{e+h} = \frac{\Delta R(t_p)}{R} \times \frac{c\varepsilon_0(n^2-1)}{2} \qquad (5)$$

which contains the electric charge q, the speed of light c, the permittivity of free space ε_0, the pump-probe delay time t_p, and the effective refractive index of the crystal at terahertz frequencies n [60].

The measured reflection change and equation (5) are based on a change in the complex refractive index of the crystal caused by the induced conductivity. However, the non-excited refractive index n also depends on the dark conductivity $\sigma = q\mu_h p_0$ as described by equation (6).

$$n^2 = {n_0}^2 + i\frac{q\mu_h p_0}{\omega\varepsilon_0} \qquad (6)$$

Using the doping concentration p_0 and hole mobility μ_h derived by Hall measurements, the second term in equation (3) is ≈ 2.3i at 1 THz. The first term, n_0^2 = 8.9, contains the contribution of refractive index of the insulating crystal, which is estimated from the sulfur-based kesterite. To derive μ_{e+h}, we combine equation (5) and (6) with the induced sheet carrier concentration and the measured ΔR/R 20 ps after excitation. The initial sheet carrier concentration $\Delta n_s = \alpha\Phi_{Ph}$ is generated by the pump photon flux, Φ_{Ph}, of 6.9×10^{12} cm^{-2} per pulse and assuming that 25% of photons are reflected. We also account for the decay of Δn_s within the first 20 ps.

The derived AC-mobility at terahertz frequencies is shown in **Figure 4**. It exhibits a real part that increases with frequency. This spectral response indicates charge carrier localization and can be modeled with the Drude-Smith model, including the localization parameter c_1 and an effective scattering time τ_{scat}, in equation (7).

$$\mu_{AC}(f) = \frac{\mu_{DC}}{1+c_1}\frac{1}{1-2\pi i f\tau_{scat}}\left(1+\frac{c_1}{1-2\pi i f\tau_{scat}}\right) \quad (7)$$

Fitting this model to our data yields a DC-value of the sum mobility of electrons and holes μ_{e+h} of 143 cm^2/Vs ±20%, which falls in the range of terahertz mobility of CZTSSe thin films [3, 61]. The localization parameter c_1 of -0.65 equals the value reported for CZTSe thin films [4]. The localization parameter scales in general from 0 for free Drude-like transport to -1 for complete localization and zero DC-mobility. Therefore, we can conclude that the carrier localization in kesterites is an intra-grain, bulk phenomenon and is possibly caused by potential fluctuation at the nanometer-scale.

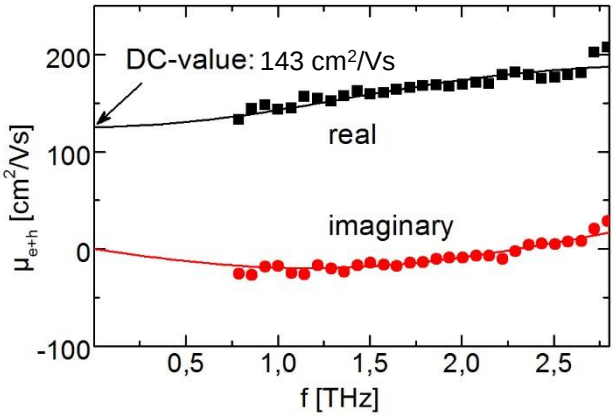

Figure 4. Sum of electron and hole mobility, μ_{e+h}, measured by TRTS 20 ps after photoexcitation by a pulse with photon flux of 6.9×10^{12} cm^{-2}. Lines show the fit with the Drude-Smith model, which enables determination of the DC mobility.

Combining the sum of electron and hole mobility derived by TRTS with the hole mobility of 89 cm^2/Vs measured by Hall effect on the same crystal, we calculate an electron mobility of 54 cm^2/Vs and an ambipolar mobility of 67 cm^2/Vs, with uncertainties in electron and ambipolar mobilities of ±30 cm^2/Vs. The results of these different methods of determining mobility are reasonably consistent with each other, especially considering that CZTSe is a highly compensated,

non-ideal semiconductor and that significant differences exist between measurement conditions: Hall effect is measured in the dark; TRTS is measured under relatively high injection; and mobility can be injection-dependent. Additionally, this electron mobility is consistent with the range of electron mobilities of 11 – 63 cm^2/Vs reported for 6.5 - 9.5% efficient thin film CZTSSe PVs [61, 62]. Further discussion of determination of carrier mobilities using terahertz spectroscopy was recently reported by Hempel, et al. Ref. X

To understand dynamics and rate-limiting mechanisms, we collected TRTS response as a function of pump fluence and wavelength, as shown in **Figure 5**. **Figure 5(a)** shows ΔR/R on a logarithmic scale and is corrected for terahertz emission that was evident in the first few

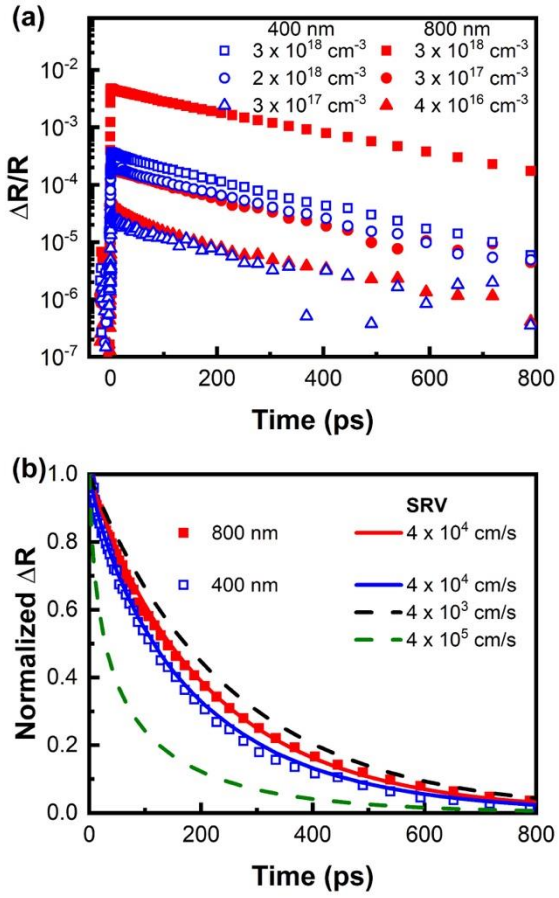

Figure 5. (a) TRTS dynamics of the crystal as a function of photoexcitation conditions, with data on log scale. (b) Normalized TRTS data (points) and best-fit model (solid lines) of 800 nm and 400 nm. The total absorbed fluence of 800 nm and 400 nm were 17 μJ/cm^2 and 10 μJ/cm^2, respectively, which give N_0 ~ 3 x 10^{18} cm^{-3} within their penetration depths. Dashed lines show the sensitivity of the model (for 400 nm excitation) to SRV, assuming SRH lifetime of 260 ps and ambipolar mobility of 67 cm^2/Vs.

picoseconds. The magnitude of the signal is proportional to the photoexcited carrier density, with assumptions mentioned previously. To first approximation, dynamics can be fit with a single exponential decay with time constant of 150 - 250 ps regardless of initial carrier profile, indicating that 1st order trapping or Shockley-Read-Hall (SRH) recombination, where $\frac{\mathrm{dn}}{dt} = -kn$, is the dominant loss mechanism. Higher order radiative recombination and Auger recombination would cause faster decay at higher pump fluence, so we conclude that these recombination mechanisms are negligible at the carrier concentrations below 3×10^{18} cm^{-3} studied here. This conclusion is consistent with our previous research on CZTSSe thin films photoexcited to similar carrier densities [3].

Interestingly, dynamics are actually a bit faster at lower fluence. These results may indicate that ambipolar diffusion, surface recombination, or bulk lifetime are injection dependent. Alternatively, this behavior may be due to trapping of photoexcited carriers at a rate controlled by both trap density and carrier density. Under high fluence conditions when the photoexcited carrier density is much larger than the trap density, full occupation of the traps would occur with relatively small impact on the large initial carrier density.

To determine the relative importance of surface recombination versus bulk trap-assisted recombination, we examined the effect of the pump wavelength on the carrier dynamics in the crystal. Pumping with shorter wavelengths, and the associated higher absorption coefficients, generates an initial carrier distribution that is concentrated closer to the front surface, promoting surface recombination. Conversely, pumping with higher wavelengths creates a more uniform carrier distribution deeper into the film, making bulk recombination more important. Under similar incident photon fluxes, dynamics are quite similar, as shown in **Figure 5(b)**, indicating that front surface recombination is not the dominant recombination mechanism. The high EQE at short wavelengths (see **Figure 1(b)**) also excludes significant front interface recombination between the CdS-buffer and the kesterite crystal in the completed solar cell.

The injection-dependent bulk lifetime makes the complete modeling of this system challenging. However, by applying the model described in the Methods section to the data in **Figure 5(b)** obtained for two wavelengths with similar high injection levels, we find an order-of-magnitude approximation of surface recombination velocity (SRV) of 4 x 10^4 cm/s and a SRH lifetime of 260 ps for bulk recombination. These parameters were derived from a global fit of the

data in **Figure 5(b)** with a shared ambipolar diffusion coefficient, SRH recombination rate constant, and SRV, but different absorption coefficients for the two pump wavelengths. We assumed that the radiative and Auger recombination terms are negligibly small and that the SRH rate equation can be simplified according to high injection conditions [63]. The high injection limit is expected to apply because the initial photoexcited carrier densities of $3x10^{18}$ cm^{-3} are much larger than the hole concentration of $9x10^{16}$ cm^{-3}. We have not modeled the data that does not fall within the high-injection limit. Such a study was recently reported by Hempel et al. Sensitivity of the dynamics to SRV is also shown in **Figure 5(b)**. While precise determination is not possible, it is clear that SRV is much smaller than 4 x 10^5 cm/s. This conclusion is consistent with values measured in CZTSe thin films [64, 65]. This approach can also enable determination of the efficacy of different surface treatments in reducing SRV [66].

The parameters obtained from TRTS can also be used to model the carrier dynamics measured by NIR-TR, using Equations 1 - 4. Because NIR-TR probes only the near-surface carriers, the carrier density decays by diffusion out of the probe depth in addition to bulk and surface recombination. In contrast, TRTS measures sheet conductivity and is sensitive to both near-surface carriers and carriers that have diffused deeper into the bulk crystal. **Figure 6** shows a fit to both data sets using the same set of parameters, supporting the consistency of our approach. **Figure S4** shows simulations of NIR-TR dynamics for other combinations of parameters to

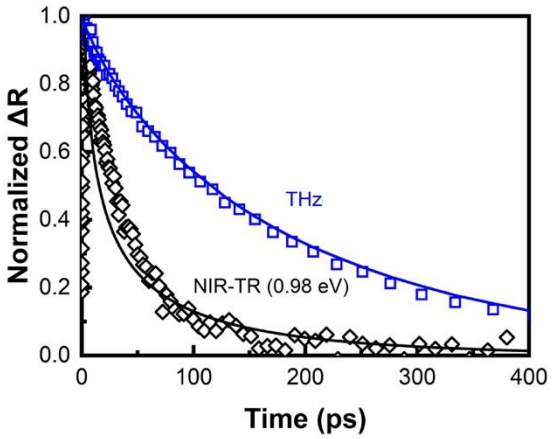

Figure 6. Dynamics of NIR-TR and THz (points) with model fit (lines). The excitation condition of NIR-TR and THz were 370 nm ($3x10^{18}$ cm^{-3}) and 400 nm ($3x10^{18}$ cm^{-3}), respectively.

provide insight into the uncertainty of the parameter estimation.

The characteristic decay time of ~200 ps from TRTS is consistent with the value that we obtained from TRPL for this single crystal and falls within the broad range reported in the literature. Phuong et al. reported TRTS dynamics of kesterite single crystals as a function of anion composition, with time constants ranging from ~ 1 ns for pure sulfide to ~50 ps for 80% selenide to <20 ps for pure selenide [37]. The lifetime of our pure selenide crystal is an order of magnitude larger. However, we have found that the cation composition strongly influences the dynamics, and Phuong et al. do not report their cation composition. Our study of cation composition will be the subject of a future publication. Polycrystalline CZTSSe thin films have frequently shown slower decays on the nanosecond scale [3, 61], in contrast to our expectation that single crystals would have longer lifetimes because of their lack of grain boundaries and secondary phases. At least three explanations may exist for this behavior. First, films grown on glass typically contain sodium, while our single crystals do not. Pure sulfide CZTS single crystals with intentional sodium doping exhibited longer lifetimes than undoped crystals [38], and the presence of sodium has also been shown to increase thin film PV device efficiency [28, 67]. Second, the slower dynamics in films may not be due to longer lifetimes, but instead to longer characteristic detrapping times, as we have previously reported [29]. The higher density of grain boundaries, and possibly point defects, in thin films may enable trapping of higher concentrations of carriers that eventually detrap and contribute to TRTS or TRPL signals. Third, the crystals may have been grown under conditions that unexpectedly favor defects that act as recombination centers.

With electron mobility of ~54 $cm^2V^{-1}s^{-1}$ and bulk lifetime of 200-260 ps, the minority carrier diffusion length is 170-190 nm. The depletion width in the CZTSe crystal of our device configuration is ~150 nm, which results in a collection length of less than 350 nm. The effect of this small collection length is evident in the EQE spectrum, **Figure 1(b**), which decreases with lower energy photons that have larger penetration depths. The small mobility-lifetime product limits the J_{sc} in our devices.

IV. CONCLUSIONS

In conclusion, knowledge of carrier dynamics obtained from multiple ultrafast spectroscopic methods can lead to improved understanding of the relationship between material properties and device performance. While our CZTSe single crystal did not have any grain

boundaries or measurable inclusions of secondary phases as are common in thin films, the charge carrier mobility was still reduced by carrier localization and the measured lifetimes were shorter than in typical polycrystalline thin films. Hence, the localized transport in kesterites is a bulk effect and can be explained by intra-grain potential fluctuations and band tails. Carriers relaxed to these tail states within ~1 picosecond and recombined within ~200 ps. This recombination has some contribution from the surface but is fundamentally limited by a short bulk lifetime. Coupled with a minority carrier mobility of 54 cm^2/Vs, this leads to diffusion length of ~200 nm. Such a short diffusion length limits carrier collection for longer wavelength photons, as evidenced in the EQE spectrum, and thereby limits J_{sc}. The similarity of the quasi-Fermi level splitting to the V_{oc} indicated that the device performance is limited by the bulk properties of the crystal.

Recent efforts to decrease the voltage deficit have focused on alloying with elements such as Ag or Ge [68-70]. This search of composition-space may be accelerated by screening with tools to measure carrier dynamics, reducing the need for the time-consuming process of making and testing devices. While described here in the context of kesterites, our approach is generalizable to many different classes of photovoltaic absorbers.

ACKNOWLEDGEMENTS

The authors acknowledge funding from a collaborative National Science Foundation grant, DMR-1507988 (Drexel Univ.) and DMR-1508042 (Univ. of Delaware). This research was also supported by the H2020 programme under the project STARCELL (H2020-NMBP-03-2016-720907). The authors thank Dr. Matthew Sfeir for assistance with NIR-TR experiments, which were performed using resources of the Center for Functional Nanomaterials, a U.S. DOE Office of Science Facility, at Brookhaven National Laboratory under Contract No. DE-SC0012704. The authors also thank Andrew Golembeski and Dr. Sergey Smolin for assistance with numerical modeling and Dr. Sukgeun Choi for sharing electronic data from Reference [58].

REFERENCES

[1] G. W. Guglietta, B. T. Diroll, E. A. Gaulding, J. L. Fordham, S. Li, C. B. Murray, and J. B. Baxter, "Lifetime, Mobility, and Diffusion of Photoexcited Carriers in Ligand-Exchanged Lead Selenide Nanocrystal Films Measured by Time-Resolved Terahertz Spectroscopy," ACS Nano **9**, 1820 (2015).

[2] W. K. Metzger, I. L. Repins, M. Romero, P. Dippo, M. Contreras, R. Noufi, and D. Levi, "Recombination kinetics and stability in polycrystalline Cu(In,Ga)Se2 solar cells," Thin Solid Films **517**, 2360 (2009).

[3] G. W. Guglietta, K. R. Choudhury, J. V. Caspar, and J. B. Baxter, "Employing time-resolved terahertz spectroscopy to analyze carrier dynamics in thin-film Cu2ZnSn(S,Se)4 absorber layers," **104**, 253901 (2014).

[4] I. L. Repins, W. K. Metzger, C. L. Perkins, J. V. Li, and M. A. Contreras, "Correlation Between Measured Minority-Carrier Lifetime and Cu(In,Ga)Se2 Device Performance," IEEE Trans. Elec. Dev. **57**, 2957 (2010).

[5] H. Tampo, K. M. Kim, S. Kim, H. Shibata, and S. Niki, "Improvement of minority carrier lifetime and conversion efficiency by Na incorporation in Cu2ZnSnSe4 solar cells," J. Appl. Phys. **122**, 023106 (2017).

[6] M. Maiberg, T. Hölscher, S. Zahedi-Azad, W. Fränzel, and R. Scheer, "Investigation of long lifetimes in Cu(In,Ga)Se2 by time-resolved photoluminescence," Appl. Phys. Lett. **107**, 122104 (2015).

[7] W. K. Metzger, D. Albin, D. Levi, P. Sheldon, X. Li, B. M. Keyes, and R. K. Ahrenkiel, "Time-resolved photoluminescence studies of CdTe solar cells," J. Appl. Phys. **94**, 3549 (2003).

[8] J. B. Baxter, C. Richter, and C. A. Schmuttenmaer, "Ultrafast Carrier Dynamics in Nanostructures for Solar Fuels," Annu. Rev. Phys. Chem. **65**, 423 (2014).

[9] J. Baxter and C. Schmuttenmaer, "Time-Resolved Terahertz Spectroscopy and Terahertz Emission Spectroscopy," in *Terahertz Spectroscopy*, S. Dexheimer, Ed. (Optical Science and Engineering: CRC Press, 2007, pp. 73.

[10] J. B. Baxter and G. W. Guglietta, "Terahertz Spectroscopy," Anal. Chem. **83**, 4342 (2011).

[11] P. U. Jepsen, D. G. Cooke, and M. Koch, "Terahertz spectroscopy and imaging – Modern techniques and applications," Laser Phot. Rev. **5**, 124 (2011).

[12] S. Ahn, S. Jung, J. Gwak, A. Cho, K. Shin, K. Yoon, D. Park, H. Cheong, and J. H. Yun, "Determination of band gap energy (Eg) of Cu2ZnSnSe4 thin films: On the discrepancies of reported band gap values," Appl. Phys. Lett. **97**, 021905 (2010).

[13] A. Walsh, S. Chen, S.-H. Wei, and X.-G. Gong, "Kesterite Thin-Film Solar Cells: Advances in Materials Modelling of Cu2ZnSnS4," Adv. Energy Mater. **2**, 400 (2012).

[14] W. Shockley and H. J. Queisser, "Detailed Balance Limit of Efficiency of p-n Junction Solar Cells," J. Appl. Phys. **32**, 510 (1961).

[15] W. Wang, M. T. Winkler, O. Gunawan, T. Gokmen, T. K. Todorov, Y. Zhu, and D. B. Mitzi, "Device Characteristics of CZTSSe Thin-Film Solar Cells with 12.6% Efficiency," Adv. Energy Mater. **4**, 1301465 (2014).

[16] M. A. Green, K. Emery, Y. Hishikawa, W. Warta, E. D. Dunlop, D. H. Levi, and A. W. Y. Ho-Baillie, "Solar cell efficiency tables (version 49)," Prog. Photovoltaics **25**, 3 (2017).

[17] S. K. Wallace, D. B. Mitzi, and A. Walsh, "The Steady Rise of Kesterite Solar Cells," ACS Energy Lett. **2**, 776 (2017).
[18] U. Rau and J. H. Werner, "Radiative efficiency limits of solar cells with lateral band-gap fluctuations," Appl. Phys. Lett. **84**, 3735 (2004).
[19] G. Rey, G. Larramona, S. Bourdais, C. Chone, B. Delatouche, A. Jacob, G. Dennler, and S. Siebentritt, "On the origin of band-tails in kesterite," Sol. Energy Mater. Sol. Cells **179**, 142 (2018).
[20] O. Gunawan, T. Gokmen, and D. B. Mitzi, "Suns-VOC characteristics of high performance kesterite solar cells," J. Appl. Phys. **116**, 084504 (2014).
[21] S. Chen, A. Walsh, J.-H. Yang, X. G. Gong, L. Sun, P.-X. Yang, J.-H. Chu, and S.-H. Wei, "Compositional dependence of structural and electronic properties of Cu2ZnSn(S,Se)4 alloys for thin film solar cells," Phys. Rev. B **83**, 125201 (2011).
[22] S. Cheng, B. Luan, and M. O. Robbins, "Contact and friction of nanoasperities: Effects of adsorbed monolayers," Phys. Rev. E **81**, 016102 (2010).
[23] T. K. Todorov, J. Tang, S. Bag, O. Gunawan, T. Gokmen, Y. Zhu, and D. B. Mitzi, "Beyond 11% Efficiency: Characteristics of State-of-the-Art Cu2ZnSn(S,Se)4 Solar Cells," Adv. Energy Mater. **3**, 34 (2013).
[24] S. Bag, O. Gunawan, T. Gokmen, Y. Zhu, T. K. Todorov, and D. B. Mitzi, "Low band gap liquid-processed CZTSe solar cell with 10.1% efficiency," Energy Environ. Sci. **5**, 7060 (2012).
[25] G. Brammertz *et al.*, "Correlation between physical, electrical, and optical properties of Cu2ZnSnSe4 based solar cells," Appl. Phys. Lett. **102**, 013902 (2013).
[26] B. Shin, O. Gunawan, Y. Zhu, N. A. Bojarczuk, S. J. Chey, and S. Guha, "Thin film solar cell with 8.4% power conversion efficiency using an earth-abundant Cu2ZnSnS4 absorber," Prog. Photovoltaics **21**, 72 (2013).
[27] I. Repins *et al.*, "Co-evaporated Cu2ZnSnSe4 films and devices," Sol. Energy Mater. Sol. Cells **101**, 154 (2012).
[28] J. V. Li, D. Kuciauskas, M. R. Young, and I. L. Repins, "Effects of sodium incorporation in Co-evaporated Cu2ZnSnSe4 thin-film solar cells," Appl. Phys. Lett. **102**, 163905 (2013).
[29] C. J. Hages, A. Redinger, S. Levcenko, H. Hempel, M. J. Koeper, R. Agrawal, D. Greiner, C. A. Kaufmann, and T. Unold, "Identifying the Real Minority Carrier Lifetime in Nonideal Semiconductors: A Case Study of Kesterite Materials," Adv. Energy Mater. **7**, 1700167 (2017).
[30] H. Hempel, T. Unold, and R. Eichberger, "Measurement of charge carrier mobilities in thin films on metal substrates by reflection time resolved terahertz spectroscopy," Opt. Express **25**, 17227 (2017).
[31] S. Chen, A. Walsh, X. G. Gong, and S. H. Wei, "Classification of Lattice Defects in the Kesterite Cu2ZnSnS4 and Cu2ZnSnSe4 Earth-Abundant Solar Cell Absorbers," Adv. Mater. **25**, 1522 (2013).
[32] D. B. Mitzi, O. Gunawan, T. K. Todorov, K. Wang, and S. Guha, "The path towards a high-performance solution-processed kesterite solar cell," Sol. Energy Mater. Sol. Cells **95**, 1421 (2011).
[33] J. M. Burst *et al.*, "CdTe solar cells with open-circuit voltage breaking the 1 V barrier," Nature Energy **1**, 16015 (2016).

[34] J. N. Duenow, J. M. Burst, D. S. Albin, D. Kuciauskas, S. W. Johnston, R. C. Reedy, and W. K. Metzger, "Single-crystal CdTe solar cells with Voc greater than 900 mV," Appl. Phys. Lett. **105**, 053903 (2014).
[35] L. Q. Phuong *et al.*, "Ultrafast free-carrier dynamics in Cu2ZnSnS4 single crystals studied using femtosecond time-resolved optical spectroscopy," Appl. Phys. Lett. **105**, 231902 (2014).
[36] L. Q. Phuong, M. Okano, Y. Yamada, A. Nagaoka, K. Yoshino, and Y. Kanemitsu, "Photocarrier localization and recombination dynamics in Cu2ZnSnS4 single crystals," Appl. Phys. Lett. **103**, 191902 (2013).
[37] L. Q. Phuong, M. Okano, G. Yamashita, M. Nagai, M. Ashida, A. Nagaoka, K. Yoshino, and Y. Kanemitsu, "Free-carrier dynamics and band tails in Cu2ZnSn(SxSe1-x)4: Evaluation of factors determining solar cell efficiency," Phys. Rev. B **92**, 115204 (2015).
[38] P. Le Quang, O. Makoto, Y. Genki, N. Masaya, A. Masaaki, N. Akira, Y. Kenji, and K. Yoshihiko, "Photocarrier dynamics in undoped and Na-doped Cu 2 ZnSnS 4 single crystals revealed by ultrafast time-resolved terahertz spectroscopy," Appl. Phys. Exp. **8**, 062303 (2015).
[39] A. Nagaoka, H. Miyake, T. Taniyama, K. Kakimoto, Y. Nose, M. A. Scarpulla, and K. Yoshino, "Effects of sodium on electrical properties in Cu2ZnSnS4 single crystal," Appl. Phys. Lett. **104**, 152101 (2014).
[40] S. Levcenko, V. E. Tezlevan, E. Arushanov, S. Schorr, and T. Unold, "Free-to-bound recombination in near stoichiometric Cu2ZnSnS4 single crystals," Phys. Rev. B **86**, 045206 (2012).
[41] I. V. Dudchak and L. V. Piskach, "Phase equilibria in the Cu2SnSe3–SnSe2–ZnSe system," J. Alloys Compounds **351**, 145 (2003).
[42] D. M. Bishop, B. E. McCandless, R. Haight, D. B. Mitzi, and R. W. Birkmire, "Fabrication and Electronic Properties of CZTSe Single Crystals," IEEE J. Photovolaics **5**, 390 (2015).
[43] M. A. Lloyd, D. Bishop, O. Gunawan, and B. McCandless, "Fabrication and performance limitations in single crystal Cu2ZnSnSe4 solar cells," in *43rd IEEE Photovoltaic Specialists Conference (PVSC)*, 2016, pp. 3636.
[44] A. Redinger, S. Levcenko, C. J. Hages, D. Greiner, C. A. Kaufmann, and T. Unold, "Time resolved photoluminescence on Cu(In, Ga)Se2 absorbers: Distinguishing degradation and trap states," Appl. Phys. Lett. **110**, 122104 (2017).
[45] M. León *et al.*, "Spectroscopic ellipsometry study of Cu2ZnSnSe4 bulk crystals," Appl. Phys. Lett. **105**, 061909 (2014).
[46] D.-H. Kuo and M. Tsega, "The investigation of CuxZnSnSe4 bulks with x=1.4–2.2 for debating the Cu excess and Cu deficiency used in thin-film solar cells," Mater. Res. Bull. **49**, 608 (2014).
[47] R. Adhi Wibowo, E. Soo Lee, B. Munir, and K. Ho Kim, "Pulsed laser deposition of quaternary Cu2ZnSnSe4 thin films," phys. stat. sol. a **204**, 3373 (2007).
[48] S. Levcenko, J. Just, A. Redinger, G. Larramona, S. Bourdais, G. Dennler, A. Jacob, and T. Unold, "Deep Defects in Cu2ZnSn(S,Se)(4) Solar Cells with Varying Se Content," Phys. Rev. Appl. **5**, (2016).
[49] J. Marquez-Prieto *et al.*, "Impact of the selenisation temperature on the structural and optical properties of CZTSe absorbers," Sol. Energy Mater. Sol. Cells **152**, 42 (2016).

[50] A. Redinger and T. Unold, "High surface recombination velocity limits Quasi-Fermi level splitting in kesterite absorbers," Scientific Reports **8**, 1874 (2018).
[51] R. K. Ahrenkiel and M. S. Lundstrom, *Minority Carriers in III-V Semiconductors: Physics and Applications*. 1993.
[52] G. W. ʻt Hooft and C. van Opdorp, "Determination of bulk minority-carrier lifetime and surface/interface recombination velocity from photoluminescence decay of a semi-infinite semiconductor slab," J. Appl. Phys. **60**, 1065 (1986).
[53] Y. Yang, Y. Yan, M. Yang, S. Choi, K. Zhu, J. M. Luther, and M. C. Beard, "Low surface recombination velocity in solution-grown CH3NH3PbBr3 perovskite single crystal," Nature Comm. **6**, 7961 (2015).
[54] A. J. Sabbah and D. M. Riffe, "Femtosecond pump-probe reflectivity study of silicon carrier dynamics," Phys. Rev. B **66**, 165217 (2002).
[55] B. R. Bennett, R. A. Soref, and J. A. D. Alamo, "Carrier-induced change in refractive index of InP, GaAs and InGaAsP," IEEE J. Quan. Elec. **26**, 113 (1990).
[56] S. Y. Smolin, A. K. Choquette, J. Wang, S. J. May, and J. B. Baxter, "Distinguishing Thermal and Electronic Effects in Ultrafast Optical Spectroscopy Using Oxide Heterostructures," J. Phys. Chem. C **122**, 115 (2018).
[57] E. A. McArthur, A. J. Morris-Cohen, K. E. Knowles, and E. A. Weiss, "Charge Carrier Resolved Relaxation of the First Excitonic State in CdSe Quantum Dots Probed with Near-Infrared Transient Absorption Spectroscopy," J. Phys. Chem. B **114**, 14514 (2010).
[58] S. G. Choi, T. J. Kim, S. Y. Hwang, J. Li, C. Persson, Y. D. Kim, S. H. Wei, and I. L. Repins, "Temperature dependent band-gap energy for Cu2ZnSnSe4: A spectroscopic ellipsometric study," Sol. Energy Mater. Sol. Cells **130**, 375 (2014).
[59] D. Hayes *et al.*, "Electronic and nuclear contributions to time-resolved optical and X-ray absorption spectra of hematite and insights into photoelectrochemical performance," Energy Environ. Sci. **9**, 3754 (2016).
[60] C. Wehrenfennig, G. E. Eperon, M. B. Johnston, H. J. Snaith, and L. M. Herz, "High Charge Carrier Mobilities and Lifetimes in Organolead Trihalide Perovskites," Adv. Mater. **26**, 1584 (2014).
[61] H. Hempel *et al.*, "Intragrain charge transport in kesterite thin films—Limits arising from carrier localization," J. Appl. Phys. **120**, 175302 (2016).
[62] T. Gokmen, O. Gunawan, and D. B. Mitzi, "Minority carrier diffusion length extraction in Cu2ZnSn(Se,S)4 solar cells," J. Appl. Phys. **114**, 114511 (2013).
[63] J. L. Gray, "The Physics of the Solar Cell," in *Handbook of Photovoltaic Science and Engineering*, A. Luque and S. Hegedus, Eds. 2 ed.: John Wiley & Sons, Ltd., 2011.
[64] C. J. Hages, N. J. Carter, and R. Agrawal, "Generalized quantum efficiency analysis for non-ideal solar cells: Case of Cu2ZnSnSe4," J. Appl. Phys. **119**, 014505 (2016).
[65] M. Patel and A. Ray, "Enhancement of output performance of Cu2ZnSnS4 thin film solar cells—A numerical simulation approach and comparison to experiments," Phys. B: Cond. Matter **407**, 4391 (2012).
[66] P. D. Antunez, S. Li, D. M. Bishop, D. B. Farmer, T. S. Gershon, J. B. Baxter, and R. Haight, "Passivation and Thickness Control of Highly Efficient Kesterite Solar Cells," Appl. Phys. Lett. **113**, 033903 (2018).
[67] C. M. Sutter-Fella, J. A. Stückelberger, H. Hagendorfer, F. La Mattina, L. Kranz, S. Nishiwaki, A. R. Uhl, Y. E. Romanyuk, and A. N. Tiwari, "Sodium Assisted Sintering of

Chalcogenides and Its Application to Solution Processed Cu2ZnSn(S,Se)4 Thin Film Solar Cells," Chem. Mater. **26**, 1420 (2014).
[68] S. Bag, O. Gunawan, T. Gokmen, Y. Zhu, and D. B. Mitzi, "Hydrazine-Processed Ge-Substituted CZTSe Solar Cells," Chem. Mater. **24**, 4588 (2012).
[69] A. D. Collord and H. W. Hillhouse, "Germanium Alloyed Kesterite Solar Cells with Low Voltage Deficits," Chem. Mater. **28**, 2067 (2016).
[70] T. Gershon, Y. S. Lee, P. Antunez, R. Mankad, S. Singh, D. Bishop, O. Gunawan, M. Hopstaken, and R. Haight, "Photovoltaic Materials and Devices Based on the Alloyed Kesterite Absorber (AgxCu1-x)(2)ZnSnSe4," Adv. Energy Mater. **6**, 1502468 (2016).